

Surface and Bulk Structural Characterization of a High-Mobility Electron-Transporting Polymer

Torben Schuettfort,[†] Sven Huettner,[†] Samuele Lilliu,[‡] J. Emrys Macdonald,[‡] Lars Thomsen,[§] and Christopher R. McNeill*,[†]

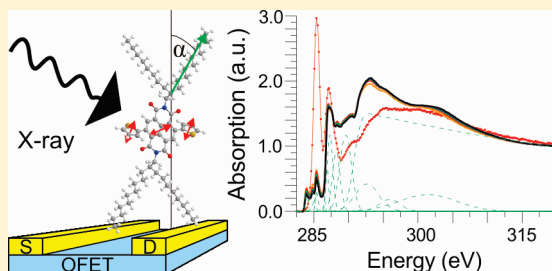
[†]Cavendish Laboratory, University of Cambridge, J.J. Thomson Avenue, Cambridge CB3 0HE, United Kingdom

[‡]School of Physics and Astronomy, Cardiff University, The Parade, Cardiff CF24 3AA, United Kingdom

[§]The Australian Synchrotron, 800 Blackburn Road, Clayton, Victoria 3168, Australia

 Supporting Information

ABSTRACT: This publication investigates the microstructure of the high electron mobility polymer poly([N,N'-bis(2-octyldodecyl)-11 naphthalene-1,4,5,8-bis(dicarboximide)-2,6-diyl]-alt-5,S'-(2,2'-12 biothiopene)) (P(NDI2OD-T2)) using a combination of grazing incidence X-ray diffraction (GIXD), near-edge X-ray absorption fine structure (NEXAFS), and optical spectroscopies. GIXD measurements confirm extended in-plane lamellae ordering and out-of-plane $\pi-\pi$ stacking. Angle-resolved surface-sensitive NEXAFS measurements, however, indicate a lack of preferred in-plane or out-of-plane orientation of either the conjugated backbone or side chains at the P(NDI2OD-T2) film surface. This lack of pronounced orientation effects is attributed to a significant proportion of amorphous content in the film, with NEXAFS measurements sensitive to both amorphous and crystalline content while GIXD is sensitive only to coherent ordering. Furthermore, it is found that increased crystallinity in annealed thin films is not beneficial to the performance of top-gate bottom-contact field-effect transistors. In fact, both highly crystalline and amorphous P(NDI2OD-T2) devices exhibit similar device performance with saturation mobilities around 0.04 and 0.02 cm²/(V s), respectively, almost 1 order of magnitude lower than the high-performance devices where the pristine morphology has not been subjected to significant heat treatment. Changes in the optical absorption and Raman spectra of P(NDI2OD-T2) thin films with annealing are also presented and discussed.



INTRODUCTION

Recent efforts to increase the performance of organic field-effect transistors (OFETs) have brought the field closer to the development of large-scale commercial applications.¹ Because of the ease of processing from solution, much focus has been placed on conjugated polymers. While high-performance p-type polymeric OFETs have been developed more than a decade ago,² generic n-type behavior in polymer OFETs has only more recently been observed that has spurred the development of high-performance electron-transporting as well as hole-transporting materials.³ Owing to their deep lowest unoccupied molecular orbital (LUMO), naphthalene diimides have shown promising potential for n-type transport^{4,5} with high electron mobilities observed in a solution processable naphthalene diimide (NDI) over a decade ago.⁶ High electron mobilities (>0.1 cm²/(V s)) in a semiconducting polymer have only been recently observed with the semiconducting copolymer poly([N,N'-bis(2-octyldodecyl)-11 naphthalene-1,4,5,8-bis(dicarboximide)-2,6-diyl]-alt-5,S'-(2,2'-12 biothiopene)), P(NDI2OD-T2).^{7,8} However, the origin of the high mobility of P(NDI2OD-T2) is not fully understood. While an early report on the material suggested that the polymer was mainly amorphous from differential scanning calorimetry (DSC) and X-ray diffraction

measurements,⁸ a recent study on thin films of the same material utilizing 2D grazing incidence X-ray diffraction (GIXD) found evidence for lamellae packing on large length scales.⁹ This lamellae packing with similar geometry had also been observed in an earlier publication on a similar material with slightly shorter side chains attached to the NDI core.¹⁰

In a paper that studied the dependence of the electron mobility on the number of thiophene units in P(NDI2OD-T₁) copolymers, all derivatives with 1, 2, or 3 thiophene rings per monomer exhibited lamellae ordering. However, it was suggested that there may be a large amorphous residue in the film.¹¹ Both crystallinity and electron mobility were found to increase when increasing the number of thiophene units from 1 to 3, although P(NDI2OD-T2) (with 2 thiophene units) exhibited a slightly larger lamellae *d*-spacing compared to P(NDI2OD-T1) and P(NDI2OD-T3). Significant changes to the electronic structure were also observed when attaching side chains to the thiophene units. While the attachment of alkyl side chains attenuated π -conjugation and increased the optical band gap,¹⁰ alkoxy side-chain substitution

Received: October 28, 2010

Revised: January 17, 2011

Published: February 14, 2011

lead to a significant reduction of the optical band gap which was further reduced through thermal annealing.¹²

In OFETs, charge transport is along the top (1 nm) layer of the semiconductor at the interface to the dielectric.¹³ In order to understand the impact of the polymer morphology on charge transport, it is therefore essential to gain insight into the local morphology at the semiconductor/dielectric interface. Since this buried interface is only accessible by very specific experimental techniques such as neutron¹⁴ or soft X-ray resonance scattering,¹⁵ this publication focuses on investigating the top surface of P(NDI2OD-T2) films using surface-sensitive techniques. Near-edge X-ray absorption fine structure (NEXAFS) spectroscopy is used as the main surface-sensitive technique that can be measured with different probing depths.^{15,16} NEXAFS spectroscopy has been a highly useful tool in determining the orientation of conjugated polymer backbones and side chains at the surface of thin films by extracting the orientation of core–shell transition dipole moments (TDMs). This has proved particularly useful for OFETs, where the measured molecular tilt angle together with X-ray scattering information has helped to provide a more accurate picture of the polymer unit cell at the charge transporting interface of the semiconductor and has been recently reviewed along with other methods used in this work.¹⁷ The molecular orientation calculated from NEXAFS spectra complements information obtained from GIXD studies that provide knowledge about coherent ordering within the film. Similar to NEXAFS spectroscopy, optical absorption spectroscopy can be utilized to characterize the electronic structure of the semiconductor bulk and provides limited information about the density of states (DOS). It has been shown that charge transport depends strongly on the alignment direction of the backbone in aligned semiconducting polymers,¹⁸ and in semicrystalline polymers charge transport also depends on the orientation of grain boundaries.¹⁹ This work aims to understand to what degree the observed crystalline structure influences the charge transport properties of P(NDI2OD-T2). The NEXAFS measurements indicate that a significant proportion of the film is amorphous, even though surface and bulk lamellae ordering is observed in agreement with previously published data.^{9,10} Furthermore, when comparing film morphology with transistor performance, it is found that peak performance does not coincide with the highest degree of crystallinity, suggesting that other factors are influencing transistor performance.

■ EXPERIMENTAL METHODS

Sample Preparation. P(NDI2OD-T2) was purchased from the Polyera Corp. (ActivInk N2200) and specified with a number-average molecular weight (M_n) and polydispersity index (PDI) of 25.4 kDa and 4.03, respectively, as determined by the supplier with gel permeation chromatography using chloroform as the solvent. Thin films were prepared by spin-coating from a 20 g/L dichlorobenzene solution in a nitrogen atmosphere. Quartz substrates were used for optical experiments and electron conducting (antimony-doped) silicon wafers for GIXD and NEXAFS measurements, the latter to avoid sample charging. The substrates were first cleaned in a subsequent acetone and 2-propanol sonic bath before oxygen plasma etch for 10 min. To analyze the bottom interface, an as-spun film was floated off its silicon substrate in deionized water and picked up with another silicon substrate with the bottom interface exposed. The film thickness was measured with a profilometer (Veeco Dektak 3) to be around 55 nm. Thermal treatment was applied in a nitrogen glovebox for 20 min at the quoted temperatures

before quickly cooling the samples to room temperature on a metal plate. All sample characterization (optical, X-ray, and electrical) was performed at room temperature.

Organic Field-Effect Transistors (OFET). A lift-off photolithographic process was used to pattern interdigitated gold source/drain electrodes with a channel length of 21.5 μm and width of 10 mm. The 25 nm thick gold source/drain electrodes were deposited via vacuum evaporation onto 1737F alkali-free glass (Präzisions Glas & Optik GmbH) with an underlying 1 nm chromium layer deposited to assist adhesion. After spin-coating and heat treatment of the P(NDI2OD-T2) layer, a 400–500 nm layer of the perfluorinated polymer CYTOP CTL-809 M (Asahi Glass) was deposited by spin-coating. A gold gate electrode was subsequently deposited by evaporation through a shadow mask. The I – V characteristics of the finished devices were measured using an Agilent 4155B semiconductor parameter analyzer with the source electrode connected to ground. All sample preparation steps were performed in a dry nitrogen atmosphere, and the sample was not exposed to air at any point between deposition of P(NDI2OD-T2) and device characterization. Saturation mobilities and threshold voltages were extracted using the gradual channel approximation:¹³

$$I = \frac{W}{2L} \mu C_i (V_g - V_t)^2 \quad (1)$$

where W is the channel width (10 mm), L the channel length (21.5 μm), C_i the capacitance per unit area (41.3 $\mu\text{F m}^{-2}$), V_g the gate voltage, and V_t the threshold voltage measured at a source-drain voltage $V_{DS} = 60$ V.

Optical Absorption and Raman Spectroscopy. The optical absorption and Raman spectra were measured on an Agilent 8453 UV–vis spectrophotometer and a Renishaw inVia Raman microscope, respectively, at room temperature. Raman spectra were acquired in a back-scattering geometry using a 532 nm laser for excitation. This excitation wavelength is between the two lowest energy absorbing resonances and allowed for the highest signal-to-noise without beam-damaging the sample.

Atomic Force Microscopy (AFM). AFM images were recorded in tapping mode on a Digital Instrument Dimension 3100, using MikroMasch NSC15, conically shaped silicon tips. Image analysis was performed with Gwyddion.

Grazing Incidence X-ray diffraction (GIXD). GIXD patterns were recorded using a multiaxis diffractometer at Beamline I16 of the Diamond Light Source, Didcot, UK. X-rays of energy of 10 keV were directed onto the sample, and the diffraction patterns recorded with a Pilatus 2M CCD detector. The measured scattering angles were calibrated to the scattering vector $q = (4\pi/\lambda) \sin 2\theta$, where λ is the X-ray wavelength and θ is the scattering angle.²⁰ Spectra were extracted from the 2D images by averaging over a 10° angle along either q_{xy} for photons scattered within the plane of the substrate or q_z for out-of-plane scattering events. All diffraction patterns presented in this work were recorded at an angle of incidence about half the critical angle of total external reflection (~0.09°) and therefore represent a measurement of the surface of the film. While the precise unit cell of P(NDI2OD-T2) and the X-ray penetration depth are not known, the penetration depth for a range of materials is generally found between 1 and 10 nm.²⁰

Near-Edge X-ray Absorption Fine Structure (NEXAFS). NEXAFS spectra at the carbon edge were recorded on the Soft X-ray Spectroscopy Beamline at the Australian Synchrotron, Victoria, Australia,²¹ where an undulator X-ray source provides nearly perfectly linearly polarized X-rays ($P \approx 1$) at a specified spectral resolution of $E/\Delta E \leq 10\,000$. The samples were placed in an ultrahigh-vacuum chamber to allow the detection of photoelectrons. The total electron yield (TEY) signal of all photoelectrons ejected from the sample was recorded via the drain current through the sample. TEY NEXAFS is surface sensitive because of the limited escape depth of the photoelectrons with measurements on poly(3-hexylthiophene) (P3HT) films determining the probing depth

to be around 2.5 nm.²² Higher surface sensitivities are obtained when measuring the Auger electron yield (AEY) signal which have an electron mean free path of less than 1 nm.^{16,22} AEY detection was performed using a SPECS Phoibos 150 hemispherical analyzer set to a kinetic energy of 230 eV. The recorded signal was normalized to the incident photon flux using the “stable monitor method”, in which the sample signal is compared consecutively to a clean reference sample and the time variations in flux measured via a gold mesh.²³ Normalization of the peak heights to an arbitrary scale was done by subtracting a background to scale the absorbance prior the onset of the first feature setting A (280 eV) to 0 and dividing by a constant to scale A (320 eV) to 1. Both the spectral normalization and the peak fitting for tilt angle extraction were performed with the Whooshka software package kindly provided by Dr. Benjamin Watts. The tilt angle of the transition dipole moment (TDM) was measured by varying the angle of incidence, θ , of the X-ray beam onto the sample. The resonance intensity of a TDM tilted by an angle α off the substrate normal can then be determined through least-squares fitting to the well-known relationship for a sample with rotational symmetry:¹⁶

$$I \propto \cos^2 \alpha \cos^2 \theta + \frac{1}{2} \sin^2 \alpha \sin^2 \theta \quad (2)$$

For carbon ring systems it has been shown that $1s(C=C) \rightarrow \pi^*$ TDMs are oriented perpendicular to the ring plane.¹⁶ For P(NDI2OD-T2) the $1s \rightarrow \pi^*$ TDM is therefore perpendicular to the NDI and thiophene ring planes, while the $1s(C-C) \rightarrow \sigma^*$ TDMs are oriented parallel to these bonds, which are predominantly found in the 2-octyldodecyl side chains.¹⁶ It is important to realize that the trigonometric squared dependency of eq 2 expresses the average of a distribution of tilt angles: A resulting tilt angle of $\alpha = 54.7^\circ$ (“magic angle”) could represent an amorphous film with random orientation of the TDMs or a film with a tilt angle at exactly 54.7° . Only when extracting tilt angles close to 0° or 90° can a narrow distribution of the molecular orientation be unambiguously inferred. Beam damage was observed as a relative change of intensity of the π^* peaks when measuring several spectra over a significant time frame in the same point of the film. This was minimized by reducing the scan time and hence reducing the overall X-ray photon exposure to a minimum and by moving to a fresh sample area for every spectrum measured. A NEXAFS transmission (bulk) spectrum was recorded at the Pollux Beamline of the Swiss Light Source, Villigen, Switzerland, for comparison.

Density Functional Theory (DFT). DFT calculations were performed using the GAMESS software package using the B3LYP functional and 6-31G*(d) basis set.²⁴ MacMolPlt was used for orbital visualizations.²⁵

RESULTS AND DISCUSSION

Optical spectroscopy is a simple way to characterize the bulk properties of an organic semiconductor. Figure 1 shows the optical absorption spectra of an as-spun P(NDI2OD-T2) thin film as well as films annealed at 110 and 210 °C or melted at 325 °C for 20 min prior to the measurement. The absorption spectra are normalized to the peak at 391 nm, which can be attributed to the $\pi-\pi^*$ transition.²⁶ The HOMO–LUMO excitation is found in the red region of the spectrum with four dominant vibronic peaks separated by ~150 meV: For the as-spun sample the lowest 0–0 peak is found at 784 nm, the 0–1 at 714 nm, 0–2 at 656 nm, and 0–3 at 606 nm as extracted by fitting Gaussian oscillators. Because of the donor–acceptor character of the respective bithiophene and NDI moieties, it is likely that this lowest optically active excitation will have a pronounced charge transfer character, similar to the well-known donor–acceptor copolymer poly[2,7-(9,9-di-*n*-octylfluorene)-co-4,7-(2,1,3benzothiadiazole)] (F8BT).²⁶

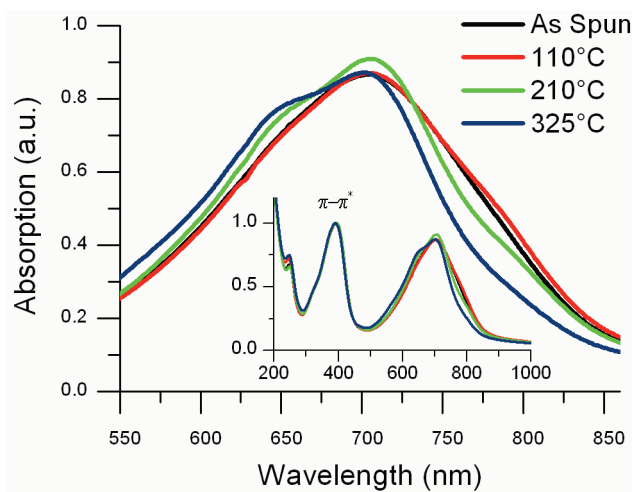


Figure 1. Optical absorption spectra of P(NDI2OD-T2) films previously annealed at different temperatures in the region of the lowest energy transition normalized to the $\pi-\pi^*$ absorption at 391 nm. A blue shift is apparent after annealing at 210 °C and melting at 325 °C. The inset shows the full spectral range of the scan.

It is interesting to note that DSC and dynamic mechanical analysis (DMA) clearly show a glass transition with an onset at about -70°C and a melt transition at $\sim 280^\circ\text{C}$ in the heating scan (see Supporting Information). Upon annealing of the as-spun film at 110 °C, there is almost no change in the absorption spectra, except for the slightest increase of the 0–0 vibronic feature at 784 nm. However, after annealing the film even higher above the glass transition temperature, the 210 °C annealed film shows a strong shift of oscillator strength from the 0–0 to the 0–1 and 0–2 vibronic features, which is even stronger after heating above the melt temperature at 325 °C. This blue shift has also been reported for a NDI-T2 derivative with a slightly shorter alkyl side chain¹⁰ but is opposite to the trend found for a derivative with dodecyloxy side chains attached to the thiophene units, where thermal treatment introduces a red shift of the absorption.¹² The reduction of the 0–0 transition can be understood as a reduction of the convoluted density of states (DOS) of the highest occupied molecular orbital (HOMO) and lowest unoccupied molecular orbital (LUMO), which indicates that either the HOMO or the LUMO has a reduced DOS for morphologies introduced via heat treatment, which is likely to influence the charge transport performance.

Raman spectroscopy is another bulk-sensitive optical technique that measures the Raman-active vibrational modes.²⁷ The raw spectra show strong variations in the form of an exponentially increasing background for higher wavenumbers. While this background is not significant for the as-spun and 110 °C sample, it becomes more prominent after annealing at 210 °C and particularly after melting at 325 °C. This background is attributed to residual photoluminescence of the film, which increases with the blue shifting of the absorption spectrum observed for the 210 and 325 °C samples. To remove the background, a fifth degree polynomial function was fitted to the data and subtracted. The background corrected and normalized Raman spectra of the as-spun, 110 and 210 °C annealed and 325 °C amorphous film are shown in Figure 2. These spectra do not show any significant shifts of peak positions and intensities, which primarily indicates that heating at high temperatures does not lead to chemical decomposition of P(NDI2OD-T2). While there are slight differences in

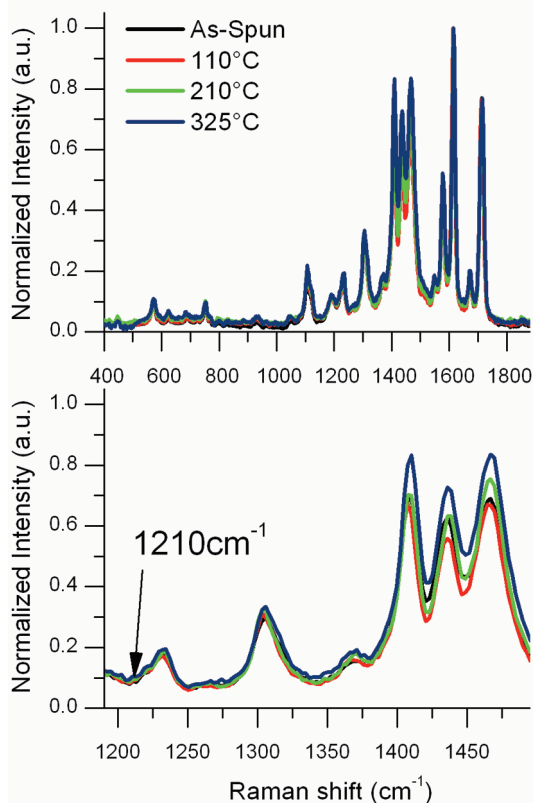


Figure 2. Raman spectra after background removal of the as-spun, 110 °C, and 210 °C annealed and 325 °C amorphous film.

the intensities of the peaks in the range 1400–1500 cm^{-1} , it cannot be ruled out that this is due to the nonlinear background normalization. However, in general, the changes in the Raman spectrum after heating are relatively minor, suggesting minimal changes in polymer conformation.

Information about the surface topography of the films can be obtained from AFM images, as shown in Figure 3. Annealing below the melt transition shows no significant change in the surface topography, which consists of fibrils of about 20–30 nm width and up to few hundred nanometers length, consistent with previous measurements.^{8,11} Local alignment of fibrils on length scales of up to 200 nm can also be observed. The extent to which these fibrils can be related to the semicrystalline structure is discussed below. It is emphasized that a fibrillar surface topography has also been observed for other NDI–thiophene copolymers, when varying the number of thiophenes¹¹ or alkoxy side chains attached to the thiophene.¹² In the former case the fibrillar morphology was most pronounced for P(NDI2OD-T2), while three thiophene units appeared to give the highest crystallinity in X-ray diffraction, largest electron mobilities, and lowest threshold voltage in FETs. After heating the sample at 325 °C, the fibrils disappear and the surface becomes flat, as expected for a frozen amorphous melt.

GIXD provides information about the coherent ordering of the crystalline domains at the surface (top ~5–10 nm) of P(NDI2OD-T2) thin films. The 340 °C melt film clearly lacks any significant pattern and can therefore be considered as entirely amorphous. The as-spun and 210 °C films, where the heat treatment has not exceeded the melt temperature, show a similar diffraction pattern, all shown in Figure 4a. When annealing the

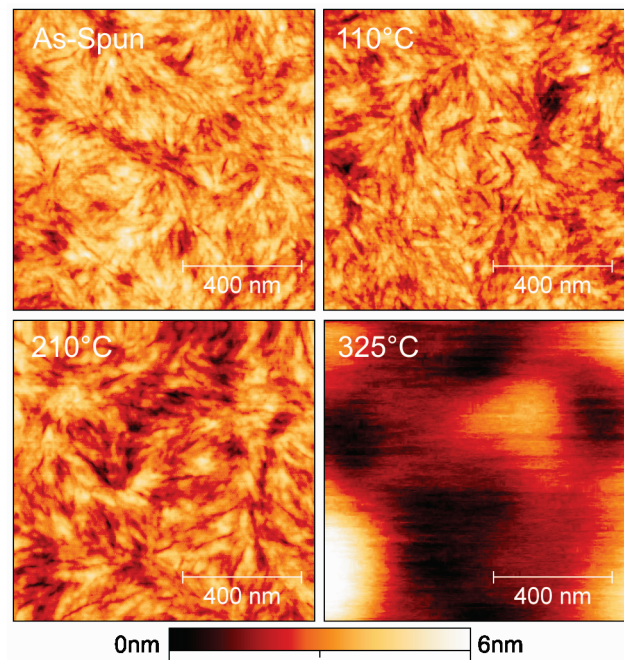


Figure 3. AFM images of the P(NDI2OD-T2) films after heating at different temperatures, showing a similar fibril-like morphology for as-spun, 110 °C, and 210 °C annealed films, while the amorphous 325 °C film shows a flat topography.

as-spun film above the glass transition temperature, the peaks in the diffraction pattern become much more defined, which can be seen more clearly by plotting the in-plane (q_{xy}) (Figure 4c) and out-of-plane (q_z) (Figure 4d) components. The as-spun, 210 °C, and 340 °C spectra are offset in parts c and d of Figure 4 for clarity.

The recorded 2D patterns and peak assignment of the GIXD measurement for surface and bulk (not shown) are similar to the ones published previously for the bulk.⁹ Since we do not observe significant differences between the bulk and surface, the data for the sample surface will be discussed in the following. The (010) π – π stacking peak is found in the out-of-plane direction at a length scale of 3.65 Å, which indicates flat-lying P(NDI2OD-T2) backbones on the substrate. A spacing of 23.4 Å is found from the lamellae (100) peaks in the in-plane direction, which is similar to the bulk values of 24.5 Å found in XRD¹¹ and 25.5 Å in GIXD.⁹ The in-plane scattering also shows the previously identified peaks in the [001] direction, which are directed along the polymer backbone at a length scale of 12.8 Å. The peak intensities at $q_{xy} = 0.96 \text{ \AA}^{-1}$ and $q_{xy} = 1.92 \text{ \AA}^{-1}$ cannot be related to higher orders of the (001) peak, which represents ordering along the backbone direction. This was previously interpreted as indication of a second polymorph (001') in the backbone direction at a length scale of 6.6 Å.⁹ While our DFT calculations identify two polymorphs with different thiophene torsional angles (vide infra), there are not enough higher order peaks to extract the precise unit cell parameters for P(NDI2OD-T2), so that it cannot be ruled out that this observation arises from the unit cell structure factor.

In order to gain information about the molecular structure, the geometries of NDI2OD-T2 dimers were optimized using DFT, where the side chains were omitted to ease computational demands. Two possible configurations of the monomer were identified: one with the thiophene pointing toward the center axis of the NDI moiety (“in” configuration) and one pointing away from this axis (“out” configuration), both shown in parts a and b of

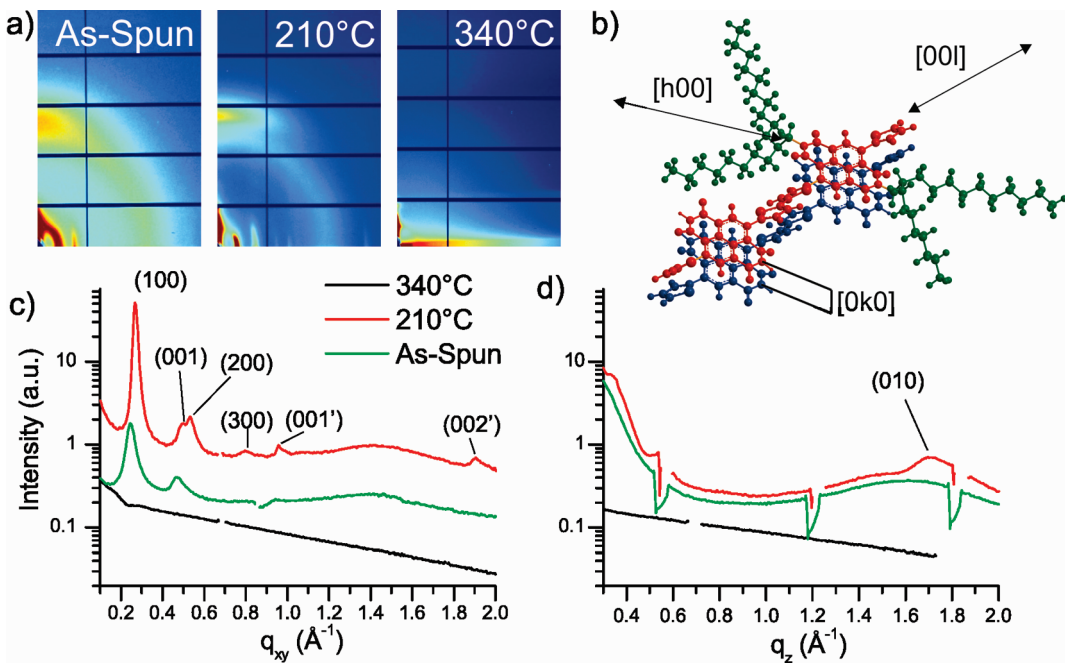


Figure 4. (a) 2D detector images of the GIXD pattern of P(ndi2od-T2) thin films previously heated at different temperatures. While semicrystalline diffraction patterns are observed for annealed films below the melt temperature, these patterns vanish for the amorphous melt. A drawing of the lamellae with two stacked backbones (blue, red), where only a single monomer has side chains (green) for clarity is sketched in (b). Furthermore, the scattering intensity of the in-plane (q_{xy}) and out-of-plane (q_z) component of the scattering vector q are shown in (c) and (d), respectively. The in-plane scans reveal peaks arising from the periodic lamellae, while the out-of-plane shows the (010) $\pi-\pi$ stacking peak.

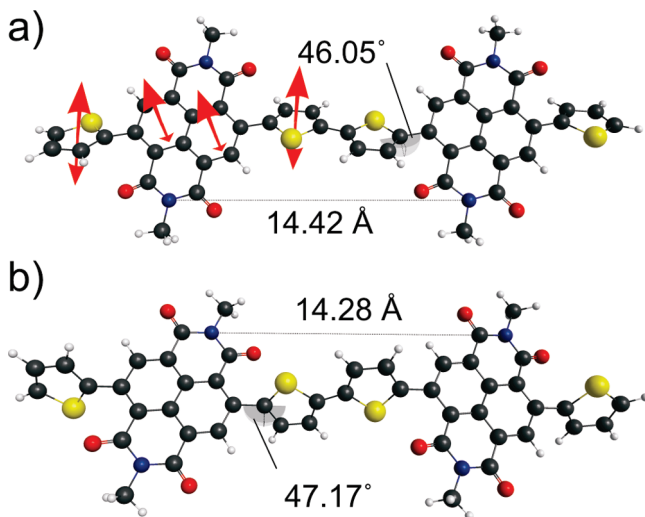


Figure 5. DFT-optimized geometries of the P(ndi2od-T2) “in” and “out” dimer configurations are shown in (a) and (b), respectively, with the vectors of the $1s \rightarrow \pi^*$ TDM (left molecule of “in” only).

Figure 5, respectively. The total energy of the “out” configuration is only ~ 2 meV smaller than for the “in” configuration, giving no energetic preference for either from these calculations. The dihedral angle between the T2 and NDI moiety and the length of one repeat unit along the backbone (001) direction are also similar for both configurations. The former angle measures 46.05° and 47.17° , while the latter distance is 14.42 and 14.28 Å for “in” and “out” configuration, respectively. The calculated values for the (001) repetition are in both cases similar to the value calculated previously⁹ but larger than the experimentally found value of 12.8 Å. A distinct difference between the two

configurations is the tilt angle of the NDI moiety with respect to the [001] direction, which is changed by $\sim 10^\circ$. The resulting packing geometry of the molecules derived from the limited information available is drawn in Figure 4b.

The size of the crystalline domains can be estimated with the Scherrer equation to be $D_L = 0.9 \cdot 2\pi \cdot (\Delta q)^{-1}$, where Δq is the full width at half-maximum (fwhm) of the peak.²⁰ When annealing the as-spun film at 210 °C, the crystalline domain size of the (100) lamellae ordering increases from 10.4 to 27.3 nm, while the extent of the (001) domains of the ordered polymer backbone only grows from 10.4 to 15.9 nm. These in-plane domain sizes are similar to the values observed in the previous publication, where a much larger (300 kDa) molecular weight was used.⁹ This is in agreement with previous observations where no dependency of the electron mobility on molecular weight was found.⁸ Furthermore, the domain sizes are similar to the width of the fibrils observed in the AFM images. While no change in the size distribution with annealing is obvious from the AFM images, this could be due to the limited lateral resolution of the instrument (conically shaped tip with 10 nm radius). Furthermore, AFM phase images (see Supporting Information) which may show a phase contrast due to different mechanical properties of crystalline and amorphous P(ndi2od-T2) do show weak phase contrast that follows the topography contours of the sample. Since for the melt sample there is no evidence for the formation of crystallites and at the same time no fibrils were observed in the AFM data (discussed above), one might speculate that the formation of fibrils is related to the crystallinity of the samples. However, fibrils could also be formed due to the slow drying of the high boiling point solvent (dichlorobenzene). The large polydispersity of the material yields a distribution of chain lengths around 36 nm (M_n) to 180 nm (M_w). This indicates that the polymer chain length is much larger than the measured domain sizes and would allow for efficient interconnection of the semicrystalline

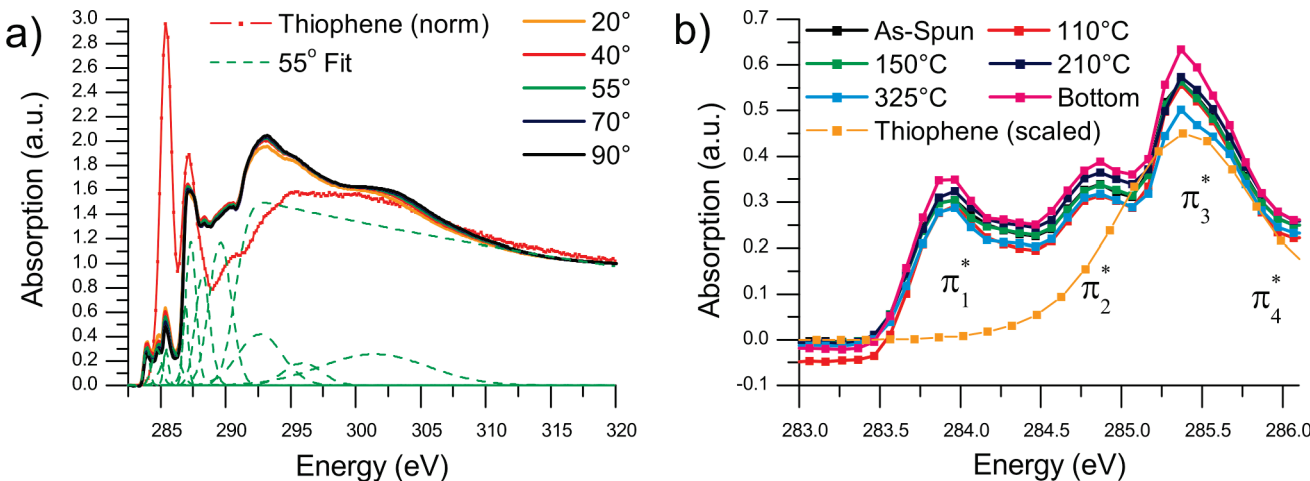


Figure 6. (a) TEY NEXAFS spectra of an as-spun P(NDI2OD-T2) film recorded at different X-ray angles of incidence and including the fitted Gaussian and step-edge functions (green) for 55° incidence. The gas-phase thiophene spectrum is shown from ref 28. The TEY measurement of the $1s \rightarrow \pi^*$ transition for different annealing temperatures at 55° X-ray incidence is shown in (b).

domains by polymer chains. The domain size of the $\pi-\pi$ stacking is 3.1 nm for the 210 °C annealed sample, which is almost exactly the same value found previously for larger M_w and indicates coherent stacking of about 8.5 molecules.⁹ The equal presence of the two configurations “in” and “out” calculated with DFT is unlikely when considering the large length scales of coherent order, but the parameters extracted from GIXD do not allow to distinguish between the two.

In order to measure the molecular orientation/degree of order at the surface of P(NDI2OD-T2) films angle-dependent carbon-edge NEXAFS spectroscopy was performed. The spectra shown in Figure 6 a) show several features in the region associated with $1s \rightarrow \pi^*$ transitions at around 285 eV. In order to identify these components, it is helpful to compare the P(NDI2OD-T2) spectrum to a spectrum of thiophene. Early NEXAFS work on thiophene showed that there are no significant alterations in the thiophene spectra when changing from the gas to the solid or monolayer phase,²⁹ but only showed shifts of the carbon 1s ionization potential. This is frequently utilized in the building block approach, where a NEXAFS spectrum of a novel compound is assembled from the spectra of its components.¹⁶ When comparing the NEXAFS spectrum of P(NDI2OD-T2) to a gas-phase spectrum of thiophene from the Gas Phase Core Excitation Database,²⁸ it seems that the peak at 285.4 eV is dominated by a core–shell transition on the thiophene moiety, while the lower energy peaks are related to transitions on the NDI moiety. While this is in agreement with the deep LUMO of NDI derivatives,^{4,5} the applicability of the building block approach is limited due to the presence of π -conjugation in P(NDI2OD-T2). However, because of the donor–acceptor character of the bithiophene and NDI moieties, it is likely that the different LUMO levels have different local charge densities and therefore different core–shell oscillator strengths. This is also indicated from the HOMO and LUMO orbitals calculated using DFT (see Supporting Information), which has recently been employed to match the calculated DOS projected onto the N and O atoms of a NDI derivative to the measured NEXAFS spectra.³⁰ While for the HOMO the charge distribution is predominantly found on the bithiophene, the LUMO exhibits a more localized charge density on the NDI moiety with the degree of localization decreasing for higher order LUMOs (see Supporting Information). This suggests

that the lowest $1s \rightarrow \pi^*$ TDM is associated predominantly with the NDI unit, while oscillator strength for higher order $1s \rightarrow \pi^*$ transitions is shifted to the bithiophene.

At an X-ray angle of incidence of 55° the spectra are independent of molecular orientation and allow for qualitative comparison of the π^* absorption intensity. The normalized TEY spectra in the region of the π^* transitions are plotted in Figure 6b. After heat treatment only a small change of oscillator strength with temperature is observed, with the melt (325 °C) showing the lowest and the as-spun bottom surface the highest π^* oscillator strength. The as-spun top-surface and 110, 150, and 210 °C samples all have similar values. For the 110 °C sample a small dip in the pre-edge region is observed only at 55° incidence, which is likely to originate from a disturbance during this particular measurement. Because of the limited energy resolution of NEXAFS spectroscopy compared to optical spectroscopy, changes in the intensity of different vibronic features with annealing cannot be resolved in the NEXAFS spectra. However, NEXAFS spectra may provide a measure of the unoccupied DOS if the ionization potential is similar for all carbon atoms.¹⁶ Because of the non-equivalent carbons in the molecule (C–N, C–O, C–C, and C–S bonds), the NEXAFS spectra presented here have to be considered a convoluted DOS from different core levels.

Measuring spectra at different angles of incidence allows for the tilt angle α of the TDMs of P(NDI2OD-T2) to be extracted. The oscillator strength for the different core–shell transitions are extracted by fitting Gaussian functions and a step function for transitions into the continuum to the NEXAFS spectra as shown in Figure 6a. By fitting the experimental absorption intensity to eq 2, it is possible to extract the average tilt angle α of the TDMs. These are drawn for the backbone (π^* transitions) and side chains (σ^* transition at 293 eV) for a P(NDI2OD-T2) monomer in Figure 7b. Figure 7a shows the theoretical dependence of the absorption intensity on the X-ray angle of incidence for TDMs tilted by $\alpha = 0^\circ$, 90° , or 54.7° of the surface normal as described by eq 2. It is obvious that for a tilt of 54.7° no dependence on the X-ray angle of incidence is observed and could therefore also represent an entirely amorphous sample.¹⁶ A total of four peaks were fitted to the π^* region, and the extracted angles for the π^* and σ^* transitions are plotted in Figure 7c for AEY and Figure 7d for TEY measurements.

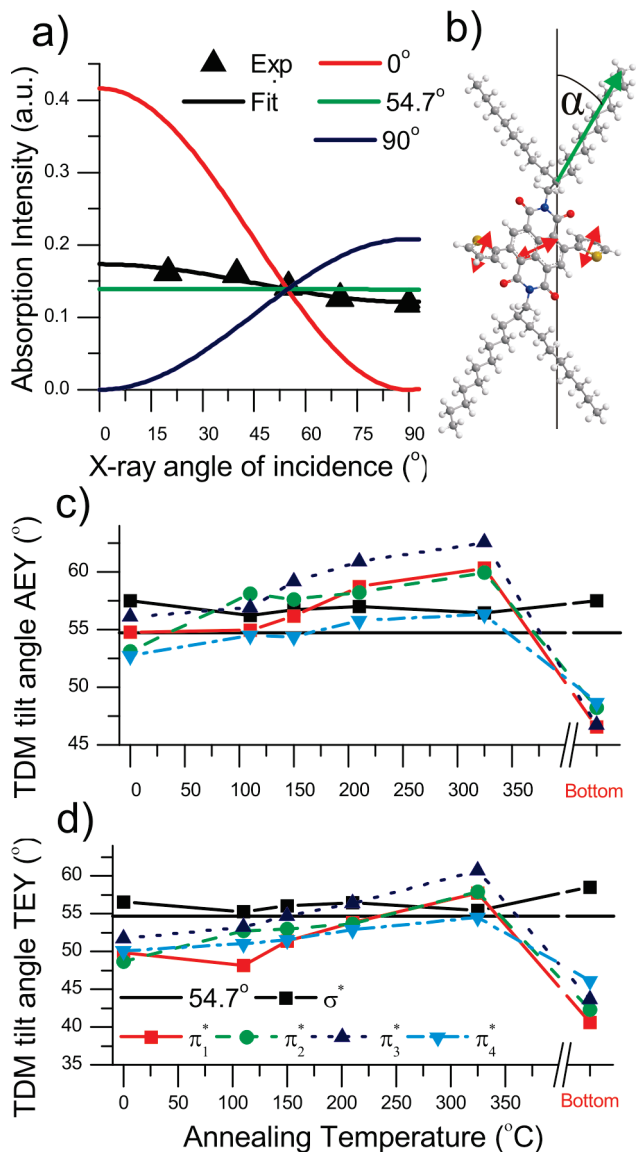


Figure 7. (a) Calculated absorption intensity as a function of the X-ray angle of incidence for tilt angles of the TDM with respect to the substrate normal (0° , 90° , 54.7°) and the fit to the experimentally determined values for α_1 in the as-spun sample. (b) Drawing of a P(ndi2od-T2) monomer with the directions of the π^* (red) and σ^* (green) TDMs. The fitted values for α from the π_1^* , π_2^* , π_3^* , π_4^* and the side chains (σ^*) are shown in (c) for AEY and for TEY in (d).

For the side chains a tilt angle $\alpha \approx 56.8 \pm 1^\circ$ is extracted for all samples in both TEY and AEY. As discussed above, this angle is close to 54.7° , which could represent all TDMs in the film tilted 56.8° or a near-random distribution. In an earlier publication it was suggested that the side chains may act as a barrier between the semiconducting backbone and the dielectric, as the electron mobility was observed to be independent of the polarity of the polymer dielectrics used.⁸ However, this would require the backbone to be packed edge-on near the surface in order to have the side chains extend away from the film, which is in contrast to the GIXD patterns which show flat lying backbones. It can therefore be concluded that the side chains are amorphous with the slightest tendency to lie in-plane ($\alpha > 54.7^\circ$), in agreement with the lamellae structure deduced from GIXD.

A more complicated picture is found for the polymer backbone. The four π^* peaks extracted from the peak fitting are found around 283.9, 284.7, 285.4, and 285.8 eV and are analyzed individually. There is only small deviance between their values for α and while there is no clear pattern for the difference between α_1 and α_2 ; on average $\alpha_3 = a + \alpha_2$ and $\alpha_3 = b + \alpha_4$ with $a = 2.3^\circ$ (1.9°) and $b = 2.6^\circ$ (4.4°) for TEY (AEY) measurements. As discussed above, because of the charge-transfer character of the LUMO, different $1s \rightarrow \pi^*$ transitions are expected to originate geometrically on different moieties of the molecule. The gas-phase DFT geometry optimizations of the P(ndi2od-T2) dimers shown in Figure 5a,b indicate a significant dihedral angle between the T2 and NDI moieties of 46.05° and 47.17° “in” and “out” configuration, respectively. Therefore, measuring the orientation of the TDM for transitions into the different LUMO levels should result in different tilt angles with a difference of 46.05° for the respective transitions. However, all transitions exhibit similar tilt angles α . This could indicate that the orientation of molecules at the surface is essentially random or that the transitions cannot actually be assigned to local absorption events on the different moieties, either because all the LUMO orbitals have significant oscillator strength on any moiety or because the difference in C 1s core-level energies mixes the different peaks in a way that they cannot be assigned to individual transitions on different moieties.

A clear trend for all π^* TDMs to larger tilt angles is observed after heat treatment at higher temperatures. For instance, α_1 increases from 49.8° (54.8°) to 57.7° (60.3°) for TEY (AEY) measurements when melting the as-spun sample at 325°C . These angles would indicate a slightly more edge-on preference for the P(ndi2od-T2) backbone. However, analogous to the discussion for the side chains above, the GIXD data give clear evidence for $\pi-\pi$ stacking in the direction of the surface normal, which would be represented by a geometrical tilt of $\alpha = 0^\circ$. From the 2D GIXD images we can plot the dependence of the $\pi-\pi$ stacking peak intensity on the angle between q_{xy} and q_z (see Supporting Information) and find that the tilt of the $\pi-\pi$ stacked platelets is $<30^\circ$, much smaller than the values found from the NEXAFS spectroscopy above ($>45^\circ$). Even in the case where the NEXAFS measurement reflects the orientation of the effective monomer transition dipole moment (i.e., the weighted average tilt angle from the NDI and thiophene units) and given a dihedral angle of $\sim 47^\circ$, the tilt angles extracted from NEXAFS ($50^\circ < \alpha < 60^\circ$) are still too large to be reconciled with the GIXD data.

Furthermore, the extracted α are lowest for the as-spun sample, which would represent the most “flat” conformation, but increases after melting the sample at 325°C to its maximum (most edge-on). Therefore, the calculated α do not seem to depend on the crystallinity of the sample, which was largest for the 210°C sample and not detectable for the melt sample. This discrepancy between the molecular geometry extracted from NEXAFS and GIXD could be explained when considering that GIXD only probes ordered crystallites. If a significant proportion of molecules in the film are actually ordered edge-on ($\alpha = 90^\circ$), but these molecules are not present in larger crystallites with coherent order, the NEXAFS would represent an average orientation of the two ($\alpha \approx 55^\circ$). In the GIXD spectra of aligned P(ndi2od-T2) thin films there is some evidence for in-plane (edge-on) $\pi-\pi$ stacking⁹ and the out-of-plane scattering data shown in Figure 4d exhibits a large background for small q_z values which might be due to out-of-plane lamellae ordering with very small domain sizes (resulting in very broad peaks). However, the tilt angles deducted from NEXAFS are close to 54.7° , which

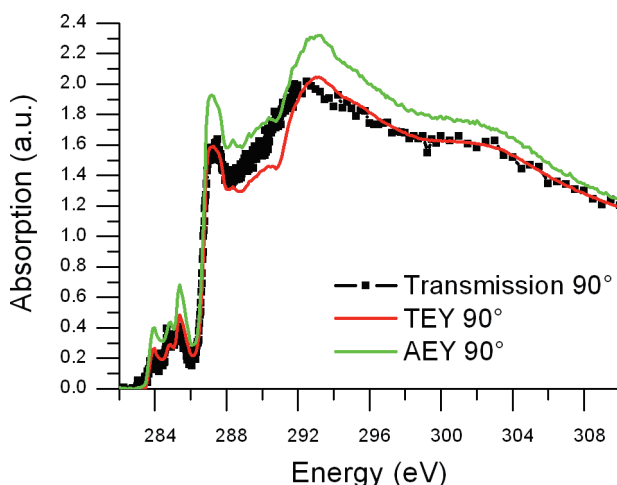


Figure 8. Comparison of the AEY and TEY NEXAFS spectra at normal (90°) incidence with the bulk (transmission) spectra.

would require equal amounts of edge-on and flat lying P(NDI2OD-T2) molecules in all the samples under investigation here. It is therefore far more likely that a broad distribution of tilt angles exists of which the extracted angle is representing merely the average. Similar to the conclusions drawn for the side chains, this data therefore indicates that the significant proportion of the polymer backbones at the surface are amorphous. Since it is not possible to determine the absolute crystallinity of the thin films, this result cannot be quantified. DSC measurements can be utilized, but since no reference values of measurable physical properties are available for purely crystalline or amorphous samples, this is not possible in this case.³¹ For P3HT a comprehensive description of the optical absorption and photoluminescence spectra in terms of an H-aggregate model allowed to extract the concentration of aggregates for films spun from different solvents to be around 40–50%.³² This is again not applicable here due to the lack of thorough understanding of the optical transitions.

On average, angles extracted from the AEY measurements are 3.9° larger than the TEY measurement. This is likely to originate from the different probing depths of the two methods. While the TEY probing depth has been determined for P3HT to be around 2.5 nm and is expected to be similar in other conjugated polymers,²² it is expected to be less than 1 nm at 300 eV for AEY measurements.¹⁶ Since the larger angles extracted for the very top surface in AEY go toward slightly larger angles than 54.7° , this would indicate that the very top surface is going toward a slightly more edge-on morphology compared to the sample fraction measured in TEY, but still with a broad distribution of tilt angles.

To understand whether the amorphous content is only present at the top surface of the film (and given the deeper probing depth in GIXD), it is instructive to compare the transmission (bulk) NEXAFS spectrum to the TEY and AEY surface spectra at the same angle of incidence (90°). These are plotted for an as-spun film in Figure 8 and show the difference between AEY and TEY, which was already discussed. The TEY and transmission spectrum are, however, essentially identical. This indicates that the information extracted from within the TEY probing depth is also representing the morphology of the bulk. If this was not the case and the bulk were to be more ordered than the layer sampled in TEY, a significant decrease in the π^* peak intensities would be expected as the flat lying molecules observed in GIXD would have a reduced oscillator strength at normal incidence. It can

therefore be concluded that ordered domains are embedded into an amorphous phase in the bulk.

A significant structural difference is found when exposing the bottom interface of the as-spun film. The molecular orientation is now changed to $\alpha_1 = 40.6^\circ$ in TEY ($\alpha_1 = 46.5^\circ$ AEY), which would represent a slightly more flat orientation that is more consistent with the GIXD results. This observation suggests that a more ordered interface is preset at the substrate/film interface. Bottom-gate top-contact transistors of P(NDI2OD-T2) on octadecyltrichlorosilane (OTS)-treated Si/SiO₂ exhibited about 1 order of magnitude lower mobilities compared to the polymer dielectric top gate devices.⁷ This might indicate that the more ordered morphology at the P(NDI2OD-T2)/SiO₂ interface is not necessarily beneficial for charge transport, although the (OTS) treated and bare SiO₂ might introduce different morphologies. Furthermore, other effects such as charge trapping at this dielectric may reduce the device performance, which would again indicate that there is no efficient shielding of the side chains between the P(NDI2OD-T2) and the dielectric.

After annealing P(NDI2OD-T2) for application in different OFET devices, distinct differences in transistor performance with annealing temperature are observed. For fabrication of OFET devices, the as-spun morphology was dried in a N₂ atmosphere at 50 °C for 30 min to remove residual solvent. When considering the minimal differences in the absorption spectra of the as-spun and 110 °C annealed film, the heat treatment at 50 °C is also not expected to introduce changes to the morphology at the given annealing temperatures. As expected, both the devices dried at 50 °C and annealed at 110 °C exhibit good transfer characteristics and mobilities comparable to the values previously published, where annealing was below 110 °C.⁸ The 50 °C device showed slightly larger hysteresis, which is likely due to residual solvent in the film. After annealing the devices at 210 °C or melting at 330 °C, the source-drain current drops and the transfer characteristics become less ideal, as seen in Figure 9a for typical devices. This is reflected in the extracted average saturation mobilities, which are plotted in Figure 9b. After annealing above 110 °C the mobilities drop by 60%–80%, while V_{th} increases from 12 V for the 110 °C to 31 and 33 V for 210 and 330 °C, respectively.

This behavior is very uncommon for OFETs, where high mobilities in semicrystalline materials are generally found for materials with in-plane $\pi-\pi$ stacking and high crystallinity,³³ whereas for P(NDI2OD-T2) the mobility drops with increased crystallinity after annealing at 210 °C. Furthermore, the mobilities and threshold voltages are similar for the melt (330 °C) and the sample with the largest crystalline domains (210 °C) as determined from GIXD. It is possible that the apparent decrease in mobility after annealing at 210 °C or melting at 330 °C is actually due to an increase in contact resistance. The contact resistance has been determined to be less than 22 kΩ cm for 110 °C annealed devices with the same channel length.³⁴ Recent evidence has been presented showing that the charge injection barrier strongly depends on the molecular orientation of a semiconducting polymer with respect to the electrode.^{35,36} A modulation of the contact resistance due to a change of P(NDI2OD-T2) morphology for increased crystalline grain size might therefore introduce the observed reduction of mobility in the case of the 210 °C sample. Furthermore, both the 210 and 325 °C sample show a significant blue shift in the absorption spectra. In the context of the mobility-edge model, which has been employed to

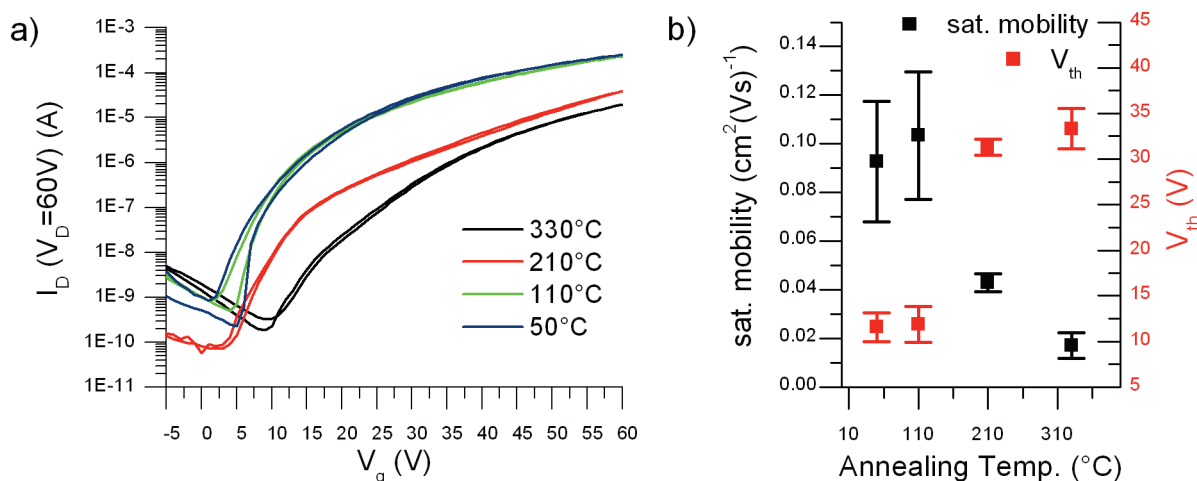


Figure 9. (a) OFET transfer curves of typical top-gate devices annealed at 50, 110, and 210 °C and melted at 330 °C. (b) Extracted mobilities and threshold voltages.

describe the mobility of high-performance organic semiconductors, a reduction of the LUMO DOS would indicate an increase of the mobility edge energy in the DOS above which charges are mobile.^{37,38} The blue-shifted absorption may therefore also indicate that the crystalline morphology, which is largest in the 210 °C sample, does not yield a DOS favorable for efficient charge transport. While it is not possible to distinguish the effects of contact resistance, bulk and interfacial transport at this point, it is clear that the device performance can neither be maximized by increasing the crystallinity nor by removing the semicrystalline ordering from the polymer altogether. Future measurements on the contact resistance, bulk mobility and activation energy in the devices may shed more light on the detailed processes involved.

CONCLUSIONS

In summary, this paper investigates the bulk and surface morphology of the high electron mobility polymer P-(NDI2OD-T2) using a combination of GIXD, NEXAFS, and optical spectroscopies. No evidence for a preferred in-plane or out-of-plane orientation of either the conjugated backbone or side chains at top surface of P(NDI2OD-T2) films is seen with NEXAFS spectroscopy. On the basis of the evidence at hand, we attribute these observations to a significant amorphous fraction of the P(NDI2OD-T2) thin films. When employing these films in top-gate bottom-contact OFETs, it is found that only the samples annealed at temperatures ≤ 110 °C yield the maximum performance. Even though significantly larger semicrystalline domains are observed when annealing at 210 °C, the saturation mobility extracted from the transfer characteristics is reduced by $\sim 60\%$. A similar behavior is observed after heating the polymer into an amorphous melt, where no semicrystalline domains can be detected in GIXD, and the saturation mobilities are reduced even further compared to the devices with pristine morphology. While the apparent reduction in the mobility of P(NDI2OD-T2) transistors after heating could be explained due to changes of the contact resistance rather than a decrease in the intrinsic mobility of the polymer, this work highlights that the high performance observed in standard P(NDI2OD-T2) devices cannot be attributed solely to the lamellae ordering within the P(NDI2OD-T2) film.

ASSOCIATED CONTENT

S Supporting Information. DSC and DMA measurements as well as further details about the DFT calculations, GIXD, and NEXAFS measurements. This material is available free of charge via the Internet at <http://pubs.acs.org>.

AUTHOR INFORMATION

Corresponding Author

*E-mail: crm51@cam.ac.uk; Tel +44 1223 337287; Fax +44 1223 764515.

ACKNOWLEDGMENT

This work was supported by the Engineering and Physical Sciences Research Council UK (EP/E051804/1). We thank Benjamin Watts for providing the Whooshka software package, for assistance when recording the P(NDI2OD-T2) NEXAFS bulk spectrum, and for helpful discussions. We also thank Ellis Pires for his assistance in recording the GIXD data sets and Gareth Nisbet and Steve Collins for their assistance on the I16 beamline at Diamond Light Source, Didcot, UK. Further thanks go to James Hugall for his assistance when recording the Raman spectra, Henning Sirringhaus and Mario Caironi for helpful discussions on P(NDI2OD-T2), and Ya-shih Huang for helpful comments on the DFT calculations. Part of this research was undertaken on the soft X-ray beamline at the Australian Synchrotron, Victoria, Australia. PolLux is funded by the BMBF (project no. 05KS7WE1).

REFERENCES

- (1) Gelinck, G.; Heremans, P.; Nomoto, K.; Anthopoulos, T. D. *Adv. Mater.* **2010**, 3778–3798.
- (2) Sirringhaus, H. *Science* **1998**, 280, 1741–1744.
- (3) Chua, L.-L.; Zaumseil, J.; Chang, J.-F.; Ou, E. C.-W.; Ho, P. K.-H.; Sirringhaus, H.; Friend, R. H. *Nature* **2005**, 434, 194–9.
- (4) Bhosale, S. V.; Jani, C. H.; Langford, S. J. *J. Chem. Soc. Rev.* **2008**, 37, 331–42.
- (5) Sakai, N.; Mareda, J.; Vauthey, E.; Matile, S. *Chem. Commun.* **2010**, 46, 4225–37.
- (6) Katz, H.; Lovinger, A.; Johnson, J.; Kloc, C.; Siegrist, T.; Li, W.; Lin, Y. Y.; Dodabalapur, A. *Nature* **2000**, 404, 478–81.

- (7) Chen, Z.; Zheng, Y.; Yan, H.; Facchetti, A. *J. Am. Chem. Soc.* **2009**, *131*, 8–9.
- (8) Yan, H.; Chen, Z.; Zheng, Y.; Newman, C.; Quinn, J. R.; Dötz, F.; Kastler, M.; Facchetti, A. *Nature* **2009**, *457*, 679–86.
- (9) Rivnay, J.; Toney, M. F.; Zheng, Y.; Kauvar, I. V.; Chen, Z.; Wagner, V.; Facchetti, A.; Salleo, A. *Adv. Mater.* **2010**, *22*, 4359–63.
- (10) Guo, X.; Watson, M. D. *Org. Lett.* **2008**, *10*, 5333–5336.
- (11) Durban, M. M.; Kazarinoff, P. D.; Luscombe, C. K. *Macromolecules* **2010**, *43*, 6348–6352.
- (12) Kim, F. S.; Guo, X.; Watson, M. D.; Jenekhe, S. A. *Adv. Mater.* **2010**, *22*, 478–82.
- (13) Horowitz, G. *Adv. Mater.* **1998**, *10*, 365–377.
- (14) Chang, S. S.; Rodríguez, A. B.; Higgins, A. M.; Liu, C.; Geoghegan, M.; Sirringhaus, H.; Cousin, F.; Dalgleish, R. M.; Deng, Y. *Soft Matter* **2008**, *4*, 2220.
- (15) Ade, H.; Hitchcock, A. P. *Polymer* **2008**, *49*, 643–675.
- (16) Stöhr, J. In *NEXAFS Spectroscopy*, 2nd ed.; Ertl, G., Gomer, R., Mills, R. L., Eds.; Springer: Berlin, 2003.
- (17) DeLongchamp, D. M.; Kline, R. J.; Fischer, D. A.; Richter, L. J.; Toney, M. F. *Adv. Mater.* **2010**, *23*, 319.
- (18) Sirringhaus, H.; Wilson, R. J.; Friend, R. H.; Inbasekaran, M.; Wu, W.; Woo, E. P.; Grell, M.; Bradley, D. D. C. *Appl. Phys. Lett.* **2000**, *77*, 406.
- (19) Jimison, L. H.; Toney, M. F.; McCulloch, I.; Heeney, M.; Salleo, A. *Adv. Mater.* **2009**, *21*, 1568–1572.
- (20) Schmidbauer, M. In *X-ray Diffuse Scattering from Self-Organized Mesoscopic Semiconductor Structures*, 1st ed.; Springer: Berlin, 2004.
- (21) Cowie, B. C. C.; Tadich, A.; Thomsen, L. *AIP Conf. Proc.* **2010**, 307–310.
- (22) Chua, L.-L.; Dipankar, M.; Sivaramakrishnan, S.; Gao, X.; Qi, D.; Wee, A. T. S.; Ho, P. K. H. *Langmuir* **2006**, *22*, 8587–94.
- (23) Watts, B.; Thomsen, L.; Dastoor, P. J. *Electron Spectrosc. Relat. Phenom.* **2006**, *151*, 105–120.
- (24) Schmidt, M. W.; Baldridge, K. K.; Boatz, J. A.; Elbert, S. T.; Gordon, M. S.; Jensen, J. H.; Koseki, S.; Matsunaga, N.; Nguyen, K. A.; Su, S.; Windus, T. L.; Dupuis, M.; Montgomery, J. A. *J. Comput. Chem.* **1993**, *14*, 1347–1363.
- (25) Bode, B. M.; Gordon, M. S. *J. Mol. Graphics Modell.* **1998**, *16* (133–8), 164.
- (26) Winfield, J. M.; Van Vooren, A.; Park, M.-J.; Hwang, D.-H.; Cornil, J.; Kim, J.-S.; Friend, R. H. *J. Chem. Phys.* **2009**, *131*, 035104.
- (27) Raman, C. V.; Krishnan, K. S. *Nature* **1928**, *121*, 501–502.
- (28) Hitchcock, A. P.; Mancini, D. C. *J. Electron Spectrosc. Relat. Phenom.* **1994**, *67*, vii–vii.
- (29) Hitchcock, A.; Horsley, J.; Stöhr, J. *J. Chem. Phys.* **1986**, *85*, 4835.
- (30) Ruiz-Osés, M.; Kampen, T.; González-Lakunza, N.; Silanes, I.; Schmidt-Weber, P. M.; Gourdon, A.; Arnau, A.; Horn, K.; Ortega, J. E. *ChemPhysChem* **2007**, *8*, 1722–6.
- (31) Bower, D. I. In *An Introduction to Polymer Physics*, 1st ed.; University Press: Cambridge, UK, 2002; Vol. 71, p 285.
- (32) Clark, J.; Chang, J.-F.; Spano, F. C.; Friend, R. H.; Silva, C. *Appl. Phys. Lett.* **2009**, *94*, 163306.
- (33) Salleo, A.; Kline, R. J.; Delongchamp, D. M.; Chabinyc, M. L. *Adv. Mater.* **2010**, *22*, 3812–3838.
- (34) Caironi, M.; Newman, C.; Moore, J. R.; Natali, D.; Yan, H.; Facchetti, A.; Sirringhaus, H. *Appl. Phys. Lett.* **2010**, *96*, 183303.
- (35) Duham, S.; Heimel, G.; Salzmann, I.; Glowatzki, H.; Johnson, R. L.; Vollmer, A.; Rabe, J. P.; Koch, N. *Nature Mater.* **2008**, *7*, 326–32.
- (36) Heimel, G.; Salzmann, I.; Duham, S.; Rabe, J. P.; Koch, N. *Adv. Funct. Mater.* **2009**, *19*, 3874–3879.
- (37) Street, R. A. In *Hydrogenated Amorphous Silicon*, 1st ed.; Cambridge University Press: Cambridge, 1991; p 417.
- (38) Chang, J.-F.; Sirringhaus, H.; Giles, M.; Heeney, M.; McCulloch, I. *Phys. Rev. B* **2007**, *76*, 1–12.